# A CT-Based High-Order Finite Element Analysis of the Human Proximal Femur Compared to In-vitro Experiments

**Zohar Yosibash**[1]
e-mail: zohary@bgu.ac.il

**Royi Padan**

Department of Mechanical Engineering,
Ben-Gurion University of the Negev,
Beer-Sheva 84105, Israel

**Leo Joskowicz**
School of Engineering and Computer Science,
The Hebrew University of Jerusalem,
Israel

**Charles Milgrom**
Department of Orthopaedics,
Hadassah University Hospital,
Jerusalem, Israel



*The prediction of patient-specific proximal femur mechanical response to various load conditions is of major clinical importance in orthopaedics. This paper presents a novel, empirically validated high-order finite element method (FEM) for simulating the bone response to loads. A model of the bone geometry was constructed from a quantitative computerized tomography (QCT) scan using smooth surfaces for both the cortical and trabecular regions. Inhomogeneous isotropic elastic properties were assigned to the finite element model using distinct continuous spatial fields for each region. The Young's modulus was represented as a continuous density function computed by a least mean squares method. p-FEMs were used to bound the simulation numerical error and to quantify the modeling assumptions. We validated the FE results with in-vitro experiments on a fresh-frozen femur loaded by a quasi-static force of up to* 1500 N *at four different angles. We measured the vertical displacement and strains at various locations and investigated the sensitivity of the simulation. Good agreement was found for the displacements, and a fair agreement found in the measured strain in some of the locations. The presented study is a first step toward a reliable p-FEM simulation of human femurs based on QCT data for clinical computer aided decision making.* [DOI: 10.1115/1.2720906]

*Keywords: finite element analysis, p-FEM, h-FEM, computed tomography, bone biomechanics*

## 1 Introduction

Predicting the mechanical response of the proximal femur for individuals is of major clinical importance as a planning and analysis tool to assist orthopaedists in treatment planning. The prediction can help surgeons determine whether a surgical or nonsurgical treatment is preferable, and, when the treatment is surgical, to choose the optimal implant type, size, or screw position. Predicting the mechanical response is nowadays very limited, as it depends on the geometrical complexity of the bone, its distinct cortical and trabecular internal regions, the anisotropic and inhomogeneous material properties which vary among individuals, and the inaccessibility to the living bone for validation. Thus, as a first step it is desirable to develop an analysis tool capable of simulating reliably the mechanical response of the proximal femur for individuals. Three-dimensional (3D) finite element analysis (FEA) for orthopaedic application has been in use for over 3 decades (Refs. [1,2] and references therein). Although the bone is a complex biological tissue, the use of FEA is attractive because at the macrolevel it exhibits elastic linear behavior for loads in the normal range of regular daily activities [3]. The proximal femur consists of cortical (compact dense and hard tissue) and trabecular (cellular spongy tissue) regions [4]. The literature reports experimentally derived homogenized mechanical properties of both regions as well as isotropic Young's modulus $E$ and other elastic constants (under the transversely isotropic/orthotropic assumption) of both regions as a function of the bone apparent density [3,5–10].

In previous FEAs of bones conventional $h$-version FE methods ($h$-FEMs) were applied, where the mesh is refined to achieve convergence whereas the polynomial degree of the shape functions is kept fixed at low-polynomial orders of $p=1$ or 2. Most of these $h$-FEMs represent the inhomogeneous distribution of material properties in the bone by assigning constant distinct values to distinct elements, thus the material properties become mesh dependent. Furthermore, the bone's surfaces are approximated by piecewise flat tesselation or piecewise parabolic tesselation, which introduces slight unsmoothness of the surface. Recent $p$-version FEMs ($p$-FEMs), on the other hand, accurately represents the bone's surfaces by using blending-function techniques, keeps the mesh unchanged and only increases the polynomial degree $p$ of the shape functions to achieve convergence and allows naturally functional variation of the material properties within each element [11]. In addition, $p$-elements are much larger, may be far more distorted, and their aspect ratio may be very large and yet produce considerable faster convergence rates compared to their $h$-FEM counterparts.

The advantages of $p$-FEMs combined with quantitative computerized tomography (QCT) data makes it possible to perform reliable simulation of patient-specific bones (see preliminary analysis of the tibia by $p$-FEMs in Ref. [12]). FE models of the femur may be created from QCT data [13–18]. The bone geometry can be obtained from the voxel coordinates, and used for generating $p$-FE patient-specific "smooth" mesh semi-automatically, including internal surfaces that separate distinct trabecular and cortical regions. A sequence of $p$-FE analyses with progressively higher accuracy and tight control of the numerical error is obtained (increasing the polynomial degree on the same geometrical mesh). QCT information can also be correlated to the local density to provide inhomogeneous, region-specific distributions of the density within the bone, used to determine a functional distribution of

[1]Corresponding author.

Contributed by the Bioengineering Division of ASME for publication in the Journal of Biomechanical Engineering. Manuscript received March 7, 2006; final manuscript received November 14, 2006. Review conducted by David Fyhrie.

  

PROOF COPY [BIO-06-1060] 001703JBY

Young's modulus $E$. The bone density at every location is estimated from Hounsfield units (HU) according to the voxels gray level and may be thereafter correlated to $E$.

The two most common methods currently in use for geometry construction and mesh generation are the voxel-based and the structure-based methods. The voxel-based method generates a FE mesh directly from the QCT data without any use of surfaces or solid bodies [19–21]. The mesh usually consists of hexahedral elements, each enclosing a predefined cubic volume containing a fixed number of QCT voxels [1]. The structure-based method generates first a geometrical model of the bone from the surface points and then automatically generates a mesh [15–18,22,23]. In general, voxel-based models are easier to automatically generate and are sufficiently appropriate to estimate deflections or interior material stresses. Structure-based models, on the other hand, are more appropriate when surface strains and stresses are of interest [1,2,18].

Both methods require the assessment and assignment of inhomogeneous mechanical properties to each element. This is usually performed by averaging the HUs of the voxels inside the finite element volume, or in a close neighborhood of the integration points [24]. In one approach, the Young's modulus in an element is derived from an averaged HU [19], which may result in underestimated mechanical properties because the $E(\mathrm{HU})$ relationship is nonlinear [19]. In another approach, the mechanical properties are first computed for each voxel and only then an averaged value is calculated [25].

Other factors that greatly influence FE results are assignment of mechanical properties to a finite element, and its size. Typically, the density is estimated by averaging the HUs within an element (density is correlated to HU using linear relations) [3,6,26,27]. This value is then used for Young's modulus estimation, usually with power-law relations [5–7,9,10,15,28]. Regarding element's size, there is usually a discrepancy between the computed tomography (CT) pixel size (about 1 mm) and element sizes (5–9 mm) used for density calculation and for mechanical properties evaluation tests. Although the influence of the element's size on the results has been reported [1,24], these studies usually focus on the computational accuracy versus meshing difficulties and computational times, with little mechanical or biological justifications for the characteristic size of elements in use. Keyak et al. reports that hexahedral 3 mm cubic elements are a good choice for a voxel based mesh [19,29]. However, Viceconti et al. show that further refinement can result in an increased error in FEA results [1]. Decreasing elements size does not lead necessarily to convergence since both geometry and material assignment change from one model to the other. Furthermore, although some studies show good experimental correlation between FE model results and fracture load, to the best of our knowledge, only two studies investigate quantitatively the differences between strains computed by FEA and and these measured experimentally on a femur bone [15,30]. In both, only partial agreement is found, suggesting the need for better simulations. In a recent FE study [2], the stresses in a femur are computed and shown to be well correlated to experimental observation. Neither displacements nor strains are reported in Ref. [2]. Similar and extensive FE analyses of vertebral bodies validated experimentally have been reported in the literature, as in Refs. [31–33] and references therein.

Herein a new structure-based modeling method is presented: smooth surfaces extracted from CT data represent the geometry and two different continuous spatial fields, independent of the mesh, are used for mechanical properties assignment in the cortical and trabecular regions (separated by an internal surface). A FE mesh was automatically constructed based on large $p$-elements [11] using blending function methods for the element mapping, thus resulting in a smooth representation of the bone surface. The mechanical properties are determined from CT data and require several steps. First, for each region (cortical or trabecular) the HU values are recalculated at each voxel using moving average [34] (see a simplified concept in Ref. [24]). Next, the apparent density ($\rho_{\mathrm{app}}$) is evaluated and a continuous spatial field, describing the density of the bone according to its coordinates, is approximated by least mean square methods (LMS). Finally the Young's modulus is represented as a smooth function in the FE analysis independent of the mesh. The thrust behind the suggested method is that the geometry is represented as accurately as possible and $E(\rho_{\mathrm{app}})$ relation is evaluated in a similar volume as the test specimens used for its estimation. Although the bone is known to be anisotropic and inhomogeneous, most studies assume an isotropic inhomogeneous material. We follow the same assumption and concentrate our attention on the geometry, mesh representation, and mechanical properties assignment for bones.

This paper is organized as follows. Section 2 describes in detail the $p$-FE mesh generation and the inhomogeneous Young's modulus determination from CT scans. An in-vitro experiment on a fresh frozen bone is also detailed. Section 3 summarizes the experiment observations, the FE results, and the various sensitivity tests performed on the model. A comparison between the FE results and experimental observations is provided. Section 4 provides an analysis of the results.

## 2 Methods

Herein we describe the proposed method for generating a $p$-FE model of the proximal femur and the procedure for identifying material parameters based on CT scans. Thereafter, the in-vitro experiments performed on human femurs to validate the FE results are described.

### 2.1 Finite Element Model and Material Parameter Assignment.

*2.1.1 Geometric Representation*. A solid model was generated based on the CT data. First, two contours defining the inner and outer bone borders at each CT slice were determined (software products Photoshop and Matlab were used) with a semi-automated procedure based on orthopaedic physician judgment.

The inner contour represents the internal border of the cortical bone and was determined only for slices where a cortical shell can be clearly visible (usually it cannot be obtained in the bone head). For the distal slices, the inner contour represents the medullar cavity surface, whereas for the more proximal slices, above the lesser trochanter, it represents the separating surface between cortical and trabecular regions. The end of the cortical region can be observed in Fig. 1.

A minimum thickness of two pixels was required for the cortical layer so as to allow meshing with tetrahedral elements. When necessary, the cortical shell was thickened but assigned with low density properties to balance it and avoid overestimating the bone stiffness.

Thereafter the external and internal smooth surfaces were approximated and a solid body was generated using the computer aided design (CAD) package SolidWorks-2004 (SolidWorks Corporation, MA). The resulting 3D solid was then imported by the $p$-FE solver StressCheck (Engineering Software Research and Development Inc. St. Louis, MO, USA) and the mesh was generated by an automesher using tetrahedral elements. The entire process is schematically shown in Fig. 2. The automesher can generate elements with either exact geometrical (blending) mapping of the physical element onto the standard element, or with a simpler, second-order polynomial mapping. Both options were used to investigate the sensitivity of the results to the mapping used in the FE analyses.

*2.1.2 Material Properties Assignment*. Bone mechanical properties were assumed to be isotropic linear elastic, with an inhomogeneous Young's modulus and a constant Poisson's ratio. This approach has been widely used in past FE studies on the proximal femur [2,14–16,19]. The isotropicity assumption is widely accepted, especially in the trabecular bone where material principal





PROOF COPY [BIO-06-1060] 001703JBY

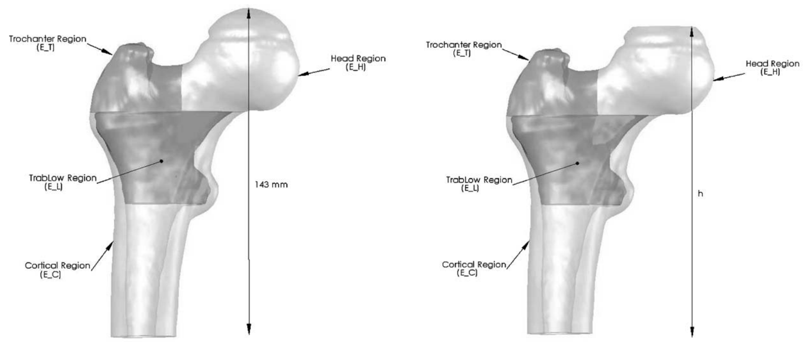


**Fig. 1 Four regions of the fresh-frozen bone model. The trabecular region was divided into three subregions, low trabecular, trochanter, and head, each with a different spatial field for the Young's modulus. In the right we show the location at which the head was trimmed to mimic the applied load in the experiment.**

directions are difficult to predict using clinical QCT protocols. To describe the bone Young's modulus, we propose to use a continuous spatial function independent of the mesh. We first applied a moving average algorithm to average the HU data in each voxel based on a predefined cubic volume surrounding it for two reasons: (a) to handle noisy discrete data; and (b) the predefined cubic volume has the same size as the specimen size used for the $E(\rho_{\text{app}})$ relation. Then, the HU averaged data in each voxel may be converted to apparent density $\rho_{\text{app}}$ using linear relations from the literature or from a phantom calibration. Next the LMS algorithm was applied to the discrete values of the apparent density which provides a continuous polynomial approximation of the density within each bone region (see the four bone regions in Fig. 1). Finally, $E(\rho_{\text{app}})$ relations were used to describe the Young's modulus as a continuous spatial function (in most other FE studies Young's modulus is constant within each element computed by the averaged data within the element).

The mentioned procedures are described in detail herein. First, the outer and inner boundaries of the bone are determined in the CT scans and HU=0 values are assigned to voxels outside the bone. The moving average algorithm sums the HU values which are greater than 0 within a cube surrounding each voxel ($S$) and divides it by the number of nonempty cells within it ($\tilde{N}$), so it does not affect nearby surface values

$$S = \sum_{i=1}^{m_1}\sum_{j=1}^{m_2}\sum_{k=1}^{m_3} \text{HU}_{ijk}, \tag{1}$$

$$\tilde{N} = \sum_{i=1}^{m_1}\sum_{j=1}^{m_2}\sum_{k=1}^{m_3} \begin{cases} 1 & \text{HU}_{ijk} > 0 \\ 0 & \text{HU}_{ijk} = 0 \end{cases} \quad \Rightarrow \quad \overline{\text{HU}}_{IJK} = \frac{S}{\tilde{N}}$$

where $i$, $j$, $k$ are the indices of voxel's position within the averaged value cube; and $I$, $J$, $K$ are indices of voxel's position within the entire CT scan data.

Subsequently, the apparent density values were evaluated based on the $\overline{\text{HU}}$ data using a linear relationship. The spatial field was approximated using LMS, finding the best-fitting function(s) closest to a given set of $N$ points by minimizing the sum of the residuals, i.e., the sum of the squares of the distances between the points and the function [35]

$$\min \sum_{i=1}^{N} [\rho_{\text{app}}^{\text{LMS}}(x_i, y_i, z_i) - \rho_i]^2 \tag{2}$$

Both Cartesian and spherical coordinate systems were considered for the spatial representation. The Cartesian system was placed at the center of the distal face of the model, and a series of polynomial functions of up to fourth degree were used to approximate the field

$$\rho_{\text{app}}^{\text{LMS}}(\text{g/cm}^3) = \sum_{i=0}^{4}\sum_{j=0}^{4}\sum_{k=0}^{4} a_{ijk} x^i y^j z^k \tag{3}$$

Additional function series were used to represent the density within the femur head, related to a spherical system where the origin was situated in the head's center

$$\rho_{\text{app}}^{\text{LMS}}(\text{g/cm}^3) = \sum_{i=0}^{3}\sum_{j=0}^{4}\sum_{k=0}^{4} a_{ijk} r^i f(j\theta) f(k\phi),$$

$$f(j\theta) = \begin{cases} \cos\left(\dfrac{j}{2}\theta\right) & \text{for } j \text{ even} \\ \sin\left(\dfrac{j+1}{2}\theta\right) & \text{for } j \text{ odd} \end{cases} \tag{4}$$

We chose four different regions in the fresh-frozen bone investigated (see Fig. 1), so that in each a different LMS approximation was obtained. The coefficients $a_{ijk}$ in Eqs. (3) and (4) for the four different regions are provided in Ref. [[36], pp. 125–127], whereas the number of points $N$ in each region are: $N^{\text{Head}} = 130{,}421$, $N^{\text{Trochanter}} = 63{,}501$, $N^{\text{TrabLow}} = 85{,}959$, $N^{\text{Cortical}} = 103{,}855$. In Fig. 3 we present on one of the CT slices the procedure described above (we chose one of the slices on which "worse approximations" was obtained).

Finally, the computed relationships $E(\rho_{\text{app}})$ were used to obtain

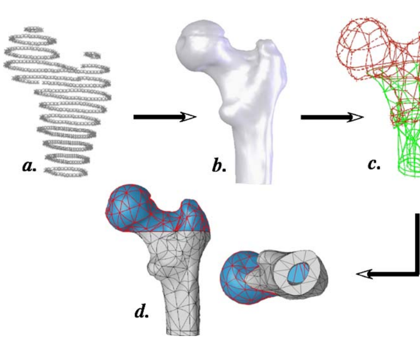


**Fig. 2 The steps for generating the *p*-FE model: (*a*) outer surface border points; (*b*) approximated smooth surface; (*c*) solid body having a cortical/trabecular separating surface; and (*d*) meshed model with two different mesh regions**

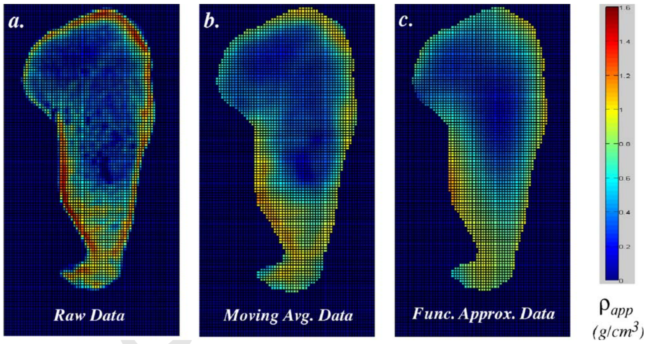


**Fig. 3 Apparent density on one of the "worse approximated" slices of the investigated bone: (*a*) $\rho_{app}$ computed from HU; (*b*) $\rho_{app}$ distribution after moving average; (*c*) $\rho_{app}^{LMS}$ represented by the LMS function**

the continuous Young's modulus representation (Table 1). Different relationships can be used for the different cortical and trabecular regions in the FE model. A constant Poisson's ratio of 0.3 or 0.4 was chosen (the sensitivity to this value is minimal, as will be shown in Subsec. 3.2.1).

Figure 4 presents the different relations for the cortical and trabecular bone. Note the large spread, especially for the trabecular bone. Although the linear elastic response of the bone is a widely accepted assumption, supported by many in-vitro experiments with a second-order visco-elastic response, the bone is definitely not an isotropic material but rather anisotropic or transversely isotropic in the cortical part. The difficulty in determining the inhomogeneous principle directions and the five required material parameters that determine Hooke's law preclude at this time a more accurate FE analysis. Nevertheless, in the authors' opinion, anisotropic material identification is one of the most prominent contributions toward a reliable FE analysis, and will be investigated in the future.

*2.1.3 FE Solver*. The resulting model was solved by the *p*-FE commercial package StressCheck. The advantages of *p*-FEMs over traditional *h*-FEMs (Ref. [11]) are: (1) the ability to describe the bone's boundary accurately as *p*-FEMs apply the blending function mapping method; (2) the possibility of using elements with very large aspect ratios—this is required in the cortical region, where elements are thin and long; (3) the possibility of monitoring the numerical error by inspecting the convergence of the results as the polynomial degree is increased over a constant mesh; (4) the possibility of providing spatial functions to describe

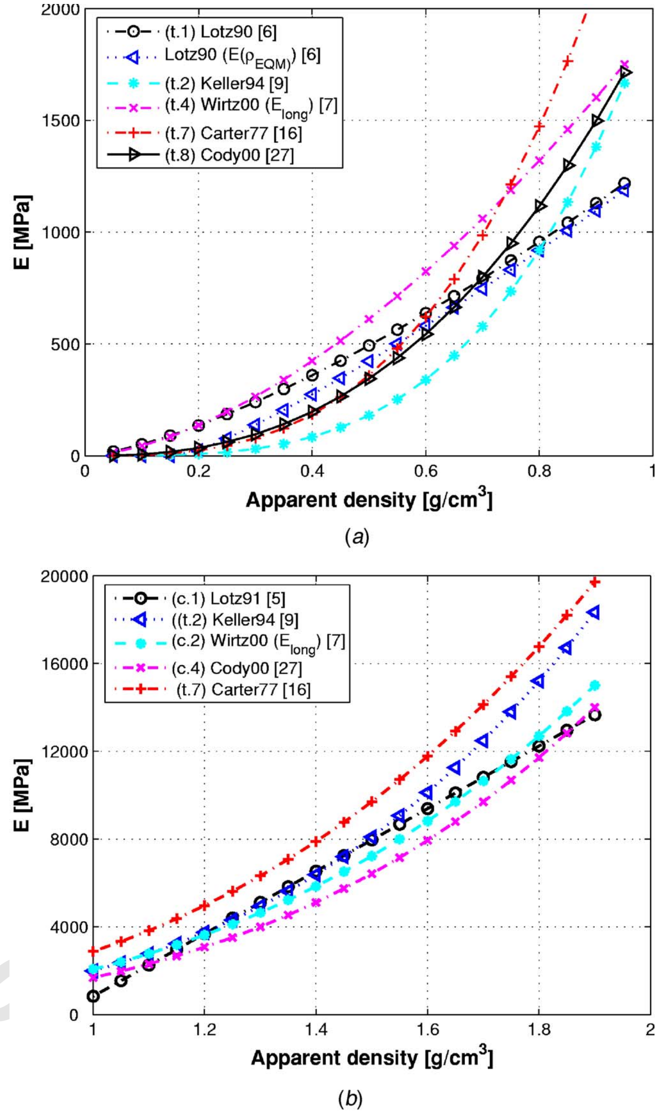


**Fig. 4 Relations between Young's modulus and apparent density as reported in past publications for the trabecular (*a*) and cortical (*b*) bone**

**Table 1 Summary of trabecular bone $E(\rho_{app})$ (MPa) relationship ($\rho$ stands for $\rho_{app}$ (g/cm$^3$))**

| Bone region | No. | $E(\rho_{app})$ Relationship | $n$[a] | $R^2$ | Testing method[b] | Specimen size | Ref. |
|---|---|---|---|---|---|---|---|
| Trabecular | (t.1) | $1310(\rho)^{1.40}$ | 49 | 0.91 | *c* | $\phi$9 mm cylinder | [6] |
| | (t.2) | $1.99\times10^3\rho^{3.46}$ | 297 | 0.75 | *c* | 8 mm cube | [9] |
| | (t.3) | $60+900\rho^2$ | — | — | *r* | — | [37] |
| | (t.4) | $1904\rho^{1.64}$ | — | — | *r* | — | [7] |
| | (t.5) | $4607\rho^{1.30}$ | 128 | 0.94 | *s* | 10 mm cube | [10] |
| | (t.6) | $3790\rho^3(d\varepsilon/dt)^{0.06}$ | 124 | — | *c* | $\phi$20.6 mm × 5 mm cyl. | [38] |
| | (t.7) | $2875\rho^3$ | — | — | *r* | — | [16] |
| | (t.8) | $1949\rho^{2.5}$ | — | — | *o* | — | [27] |
| Cortical | (c.1) | $-13{,}430+14{,}261\rho$ | 123 | 0.62 | *b* | $7\times5\times0.18\div0.4$ mm$^3$ | [5] |
| | (c.2) | $2065\rho^{3.09}$ | — | — | *r* | — | [7] |
| | (c.3) | $14\times10^3\rho-6142$ | 96 | 0.77 | *s* | ≈5 mm cube | [10] |
| | (c.4) | $1684\rho^{3.3}$ | — | — | *o* | — | [27] |

[a]Number of specimens.
[b]*c*=compression, *b*=bending, *s*=ultrasonic, *o*=quoting other source, *r*=recalculated based on published data.

the inhomogeneous material properties within any element; and (5) a considerably higher convergence rate compared to $h$-FEMs. In our studies, the degree of the polynomial of the shape functions ($p$ level) is increased from 1 to 5. Different loads and boundary constrains can be defined which will be described in the sequel for each model separately (see Fig. 4).

**2.2 Fresh-Frozen Proximal Femur FE Model.** A FE model of the fresh-frozen proximal femur was created from a CT scan acquired beforehand. The scans were performed on a Phillips Brilliance 16 CT (Einhoven, Netherlands) with following parameters: 140 kV p, 250 mA s, 0.75 mm slice thickness, axial scan without overlap, with pixel size of 0.78 mm (512 pixels covering 400 mm field size). The CT data were segmented and a solid model was constructed according to the described method. A planar face was defined to determine the height of the applied force. The femur head was trimmed according to this plane prior to mesh construction using the automesher (see right picture in Fig. 1 for which $h=137.3$ mm). Four different regions were defined so in each one a different field is used for the density's evaluation, one for the cortical region and three for the trabecular region (Fig. 1).

A linear interpolation correlating the value for water ($\mathrm{HU} \approx 0$) to $\rho_{\mathrm{app}}=0\ \mathrm{g/cm^3}$ and the maximum bone HU value of 1700 (there were very few HU values above 1700) to maximum bone density $\rho_{\mathrm{app}}=1.9\ \mathrm{g/cm^3}$ (as used by Refs. [24,28])

$$\rho_{\mathrm{app}}(\mathrm{g/cm^3}) = 1.9\frac{\mathrm{HU}}{1700} \tag{5}$$

Density evaluation based on the $K_2HPO_4$ phantom present in the CT scan [39] resulted in similar results as Eq. (5) after adjusting the equivalent mineral density to apparent density. In what follows the relation in Eq. (5) was used. A moving average was then computed using a cube containing $7\times7\times7$ voxels (edge size $\approx 5.4$ mm) for the trabecular region and a box containing $3\times3\times7$ voxels for the cortical region. The cube sizes represent a similar volume to the smallest specimens considered in the studies on $E(\rho_{\mathrm{app}})$. To appropriately approximate the apparent density in the trabecular region with a polynomial function, it was first divided into three parts: head, greater trochanter, and low trabecular regions (Fig. 1), each of them having a different function for spatial representation of density ($R^2=0.977-0.982$). One cortical and two trabecular regions were described in Cartesian coordinates, whereas femur head spatial field was described in a spherical coordinate system situated in head's center.

To investigate the sensitivity of the FE analysis, several $E(\rho_{\mathrm{app}})$ relationships were considered (Table 1). The following combinations of cortical and trabecular relations were investigated:

(1) Wirtz et al.: Different relationships for cortical and trabecular regions according to (t.4) & (c.2);
(2) Lotz + Wirtz: Cortical region properties are assigned according to (c.2). Trabecular properties are assigned according to (t.1);
(3) Carter and Hayes: Same relationship is used both in cortical and trabecular regions. A strain rate of 0.01 $\mathrm{s}^{-1}$ is used in (t.6) resulting in (t.7);
(4) Cody et al.: Different relations are assigned to trabecular and cortical regions according to (t.8) and (c.4); and
(5) Keller: Keller's relation (t.2) is used in both regions of bone.

Lotz's linear relation for cortical region (c.1) was not considered because it leads to negative Young's modulus in some parts of the cortical spatial field where the density value was lower than 0.942 $\mathrm{g/cm^3}$. Other relations used in Refs. [13,2] were not used herein because they were based on ash density and not on apparent density.

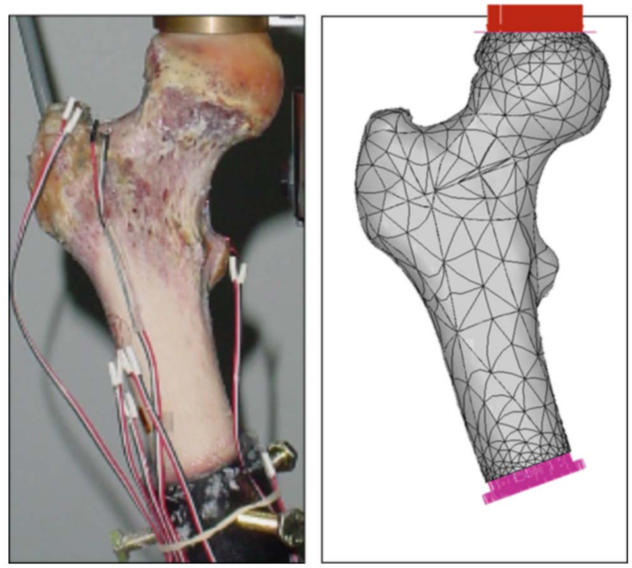

**Fig. 5 Femur under load and representing FE model. Load is applied at an angle of 20 deg to the shaft axis.**

For the sensitivity and verification analyses (documented in Subsection 3.2.1) the boundary conditions on the femur's head were taken as 1 mm displacement in the direction of the inclination angle with zero displacements in perpendicular directions. As in Ref. [27], a constant Poisson's ratio of 0.3 was used for the entire bone model, and the sensitivity of the results to this particular value was also checked.

To reproduce the loading experiment, we clamped the distal face of the bone at the location where it resides in the PMMA, and applied a pressure load, with a resultant of 1500 N enforcing zero displacement in transverse directions of the load—see Fig. 5. These boundary conditions best describe the effect of the pressing configuration assembled from a ball and a socket joint, see Fig. 5.

**2.3 In-Vitro Experiments.** To assess the reliability of the proposed FE model, we conducted two experiments on proximal femur specimens. The first was on an embalmed bone to validate the experimental procedure. The second was on a fresh-frozen femur within a period of 36 h after defrosting. In both, we measured the displacements and strains under various loading configurations.

The preliminary test on an embalmed femur of a 56 year old female was conducted to ensure proper functionality of the experimental instrumentation and determine the fracture load. Bone mechanical response showed linear response and had very good repeatability. To ensure that the fresh-frozen bone will withstand the loading, the embalmed bone was subject to an increasing load until breakage at $\sim$4000 N. The first evidence of fracture occurred at 2020 N. Consequently, a maximum load of 1500 N was determined for the fresh-frozen femur experiment.

The experiments on the fresh- frozen femur are detailed in Subsection 2.3.2.

*2.3.1 Experimental System.* The experimental system includes a mounting jig, loading, and measurement equipment, and data acquisition equipment. The experiment was performed using a displacement controlled machine (Instron 1115). The bone mounting jig was positioned on the Instron lower platform as shown in Fig. 6. The jig was designed so as to allow bone clamping at several discrete inclination angles. The bone shaft was first positioned inside a steel cylinder (2) using six screws and fixed by embedding it into polymethyl-methacrylate (PMMA). The steel cylinder was welded to a flat plate positioned on a slider with its



PROOF COPY [BIO-06-1060] 001703JBY

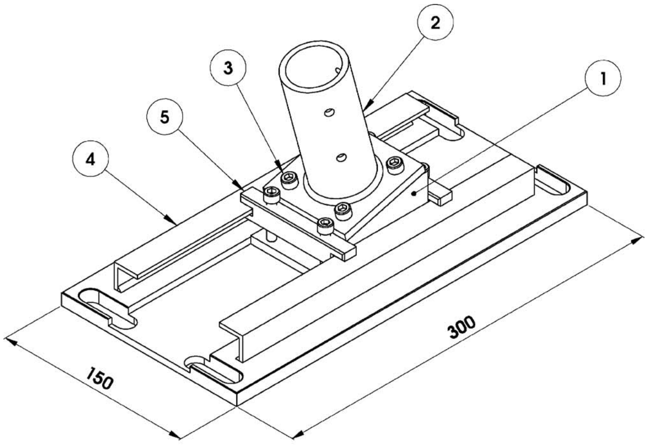


(*a*)

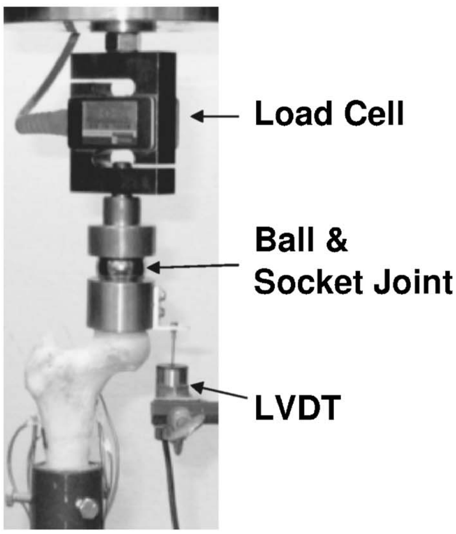


(*b*)

**Fig. 6 (*a*) Bone mounting jig (dimensions in mm): (1) slider - controls the bone's inclination angle; (2) steel cylinder (3) 4× M6 bolts (4) base and rail (5) stopper. (*b*) Load and displacements measurements (embalmed bone): Load cell, ball, and socket joint for load transmission and the LVDT.**

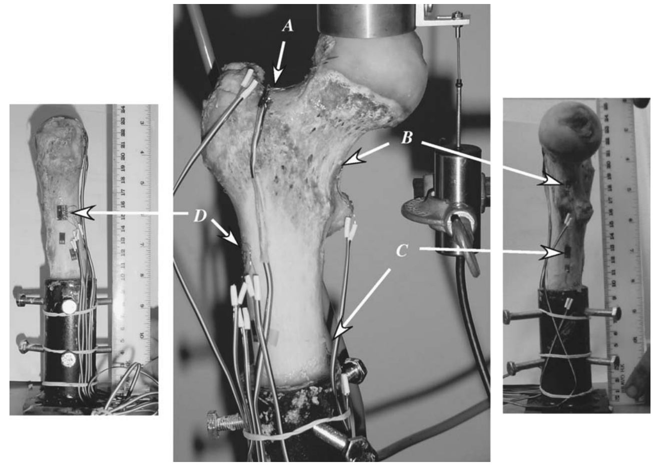


**Fig. 7 Strain gauges locations: (*A*) neck superior, (*B*) neck inferior, (*C*) shaft medial, and (*D*) shaft lateral**

top face inclined to the required angle. Sliders with different slope angles position the bone in different inclination angles and allow femur head positioning directly below the load cell.

A Tedea-616 load cell with a load error $\leqslant 0.05\%$ was used. A ball and socket joint with a steel ball between two brass cones was used to prevent moments acting on the load cell (Fig. 6). A Solartron DFg5 direct current linear variable displacement transducer (DC-LVDT) measured the femur head vertical displacement. It was positioned on a stand arm with its core connected to the brass double-cone interface on the femur's head (Fig. 6).

Strains were measured at four locations: two on the inferior and superior parts of the femur neck, and two on the medial and lateral femur shaft (Fig. 7). A rosette (Vishay CEA-06-062UR-350), positioned on the lateral side of the shaft, and three uniaxial strain gauges (Vishay CEA-06-062AQ-350) with 1.6 mm active length and 350 $\Omega$ resistance were positioned at measurement locations.

The strain gauges were connected to an eight-channel amplifier containing Vishay 2110B and four 2120B components. An eight-channel analog/digital (A/D) converter (WaveBook/516 by IO-Tech) was used. Six channels were assigned for the strain gauges: one for the load cell, and one for the LVDT readings. A sample rate of 10 HZ was used in all experiment to obtain measurement samples of less than 1 $\mu$m displacement intervals for a testing machine velocity of 0.5 mm/min. This high sample rate provides a good continuous signal with low noise. The A/D converter was connected to a laptop (Intel Pentium 4, 1.80 GHz, 256 MB) through a LAN connection.

*2.3.2 Fresh-Frozen Femur In-vitro Experiments*. A fresh-frozen femur of a 30 year old male donor was deep frozen shortly after death. To ensure no skeletal diseases of the bone the general medical history of the donor was obtained showing no major medical diseases. An x ray of the bone was taken which showed no bony lesions present. Bacterial and viral cultures were taken and were negative. After defrosting, soft tissue was removed from the bone by a combination of sharp and blunt dissection. The bone was degreased with ethanol. At the sites with minimal curvature on which strain gauge are to be applied, the bone was roughened with 400 grit sandpaper and again cleaned with ethanol. Strain gauges were serially bonded to the bone using M-Bond 200 Cyanoacrylate Adhesive (Measurements Group, Inc., Raleigh, NC, USA). Once mounted, the entire rosette gauge and its lead wires were sealed with a nitrile rubber coating (M-Coat B, Measurements Group, Inc., Raleigh, NC, USA).

The bone was affixed with six bolts to the cylindrical sleeve and fixed by PMMA. Thereafter two CT scans were acquired. The mechanical experiments started 6 h after bone mounting, long enough for PMMA to cure. During the bone preparation it was hydrated and stored in a cold humid container between the different tests. The experiments simulate a simple stance position configuration in which the femur is loaded through its head. In this loading condition, the force is applied in an inclination of $\approx 7$ deg to the shaft axis [40], along a virtual line that connects the femur head to the middle cavity in the femur diaphysis (intercondylar fossa). A total of four inclination angles were considered: 0 deg for maximal sensitivity, 7 deg as in the natural stance posture, and 15 deg and 20 deg as in Keyak et al. [30]). Forces of up to 1500 N were applied, corresponding to more than half an average body weight but smaller compared to bone's linear response regime.

The mechanical experiments lasted for 2 days. One procedure from the first day (1500 N load at 7 deg inclination) was repeated at the start and at the end of the second day to verify that bone's mechanical response (and therefore its mechanical properties) did not change. The bone was kept in refrigeration overnight.

In the experiments during the first day, the load was increased monotonically at a slow displacement rate of 0.5 mm/min. Maximum loads were 500 N, 1000 N, 1500 N, applied to each of the



PROOF COPY [BIO-06-1060] 001703JBY

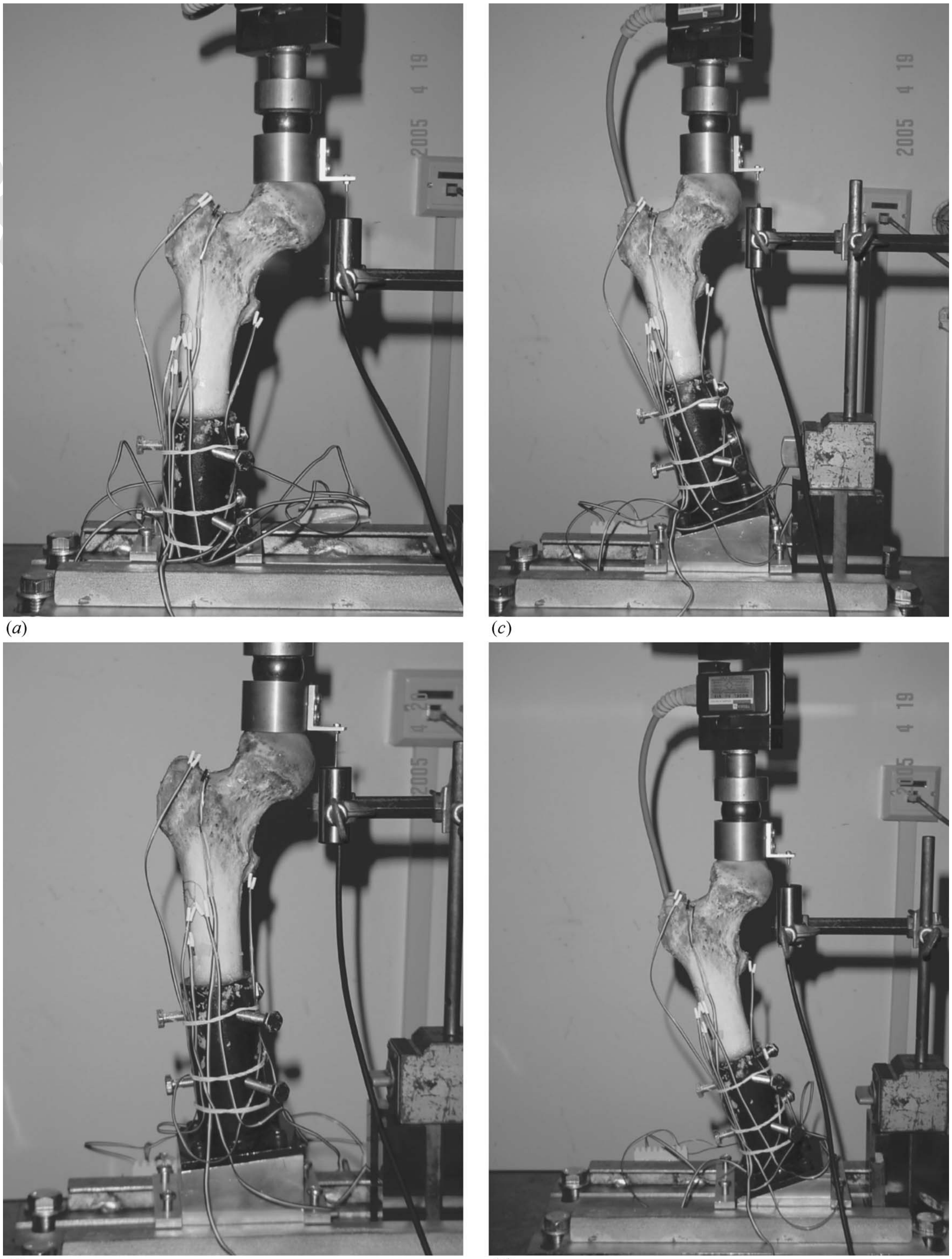


**Fig. 8 Experiments on fresh–frozen bone at different inclination angles (from *a* to *d*): 0 deg, 7 deg, 15 deg, 20 deg**

four inclination angles (see Fig. 8). Each load case was repeated twice not in a random fashion, performing 24 experiments for the 12 possible combinations (three loads and four inclination angles). The bone was kept in the fixture for the six experiments for each inclination angle. To explore the mechanical response sensitivity to the strain rate 15 more experiments were performed in the second day in which we applied 1500 N load on the femur at 7 deg inclination at several displacement rates from 0.1 mm/min to 2 mm/min. We also performed one test at 15 deg inclination to ensure that the visco-elastic response is negligible. In this test we applied a displacement on the femur's head resulting in a 1500 N force. The displacement was kept fixed for 40 s while we monitored the relaxation in the measured load. Then the additional displacement to compensate for the decreased load was measured.



PROOF COPY [BIO-06-1060] 001703JBY

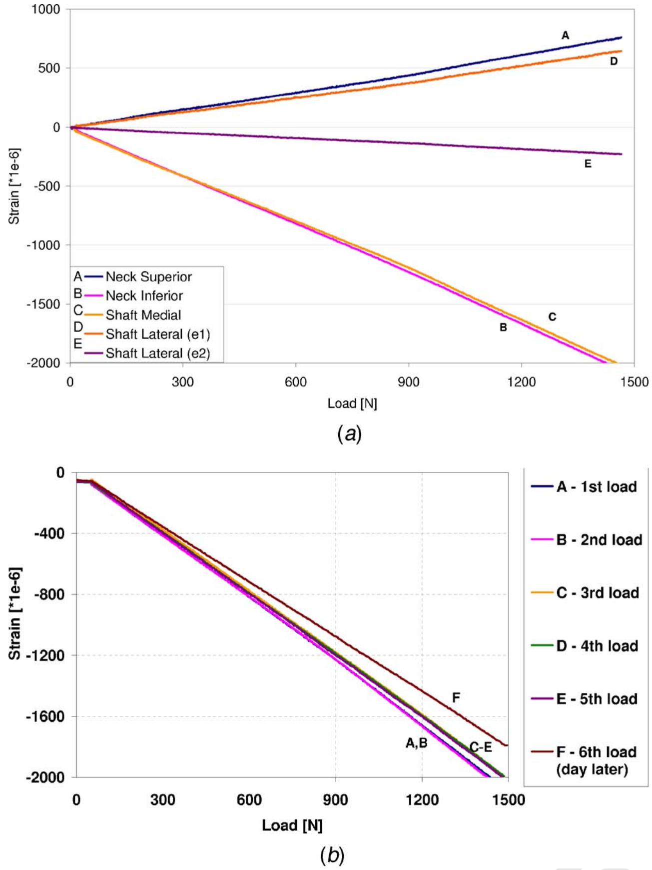


**Fig. 9 Fresh-frozen bone at 7 deg inclination under 1500 N load: (*a*) Different strain gauges versus load; (*b*) strain (neck superior) versus load at neck inferior**

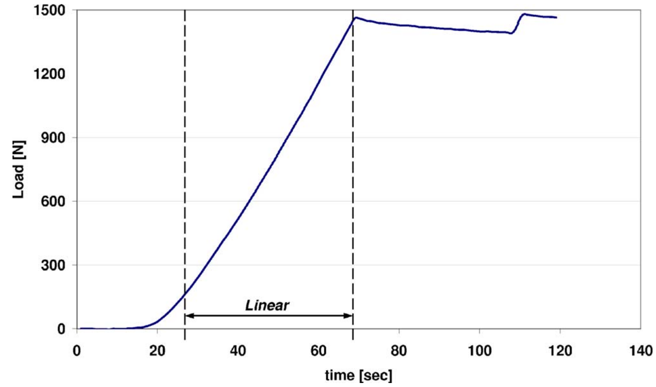


**Fig. 10 Fresh-frozen load vis. time response for 1500 N load at 15 deg inclination. Linear response is noticed after 200 N preload.**

## 3 Results

### 3.1 In-vitro Experimental Results for the Fresh-Frozen Bone.

*3.1.1 Linearity and Repeatability*. A linear response was observed after 200 N preload (Fig. 10) in all test results. Strain gauges show linear response to load ($R^2 > 0.998$) and good repeatability in the entire measurement range (see for example Fig. 9). For each inclination angle neither the bone nor the fixtures were removed from the Instron machine in between adjacent tests (except for one test at 7 deg that was performed again on the next day), and adjacent measurements show a difference of up to 5%. The maximum difference varies from 3% to 19% for different measured parameters. The two possible reasons for the difference are changes in the bone's properties due to elapsed time or small changes in the precise location at which the load was applied to the bone.

*3.1.2 Viscoelasticity*. Two indications of visco-elastic behavior were noticed. One was the strain measured as a function of applied force: the unloading curve was not identical to the loading one. The other indication was the load decrease as time passed after a given displacement was applied as shown in Fig. 10. Similar behavior was also reported by Keyak et al. [30]. In a few cases, an extra displacement of $\approx 0.05$ mm was applied to compensate for the load decrease as seen in Fig. 10 (5% during 40 s).

*3.1.3 Strain-Rate Influence*. Displacement rates in the range of 0.1–2 mm/min, equivalent to 2.3–46 $\mu$strain/s in the neck superior strain gauge or 6.8–130 $\mu$strain/s in the shaft medial strain gauge were applied. The strain rate differences were expected to introduce a 20% difference in bones stiffness according to (t.6). However, no such sensitivity was observed. Displacement and strain response to monotonic loading was almost identical at all rates measured (Fig. 11).

*3.1.4 Inclination Angle Influence*. Experiments with different inclination angles of the bone yielded consistent results except for the 7 deg inclination where a higher strain to load ratio than at the

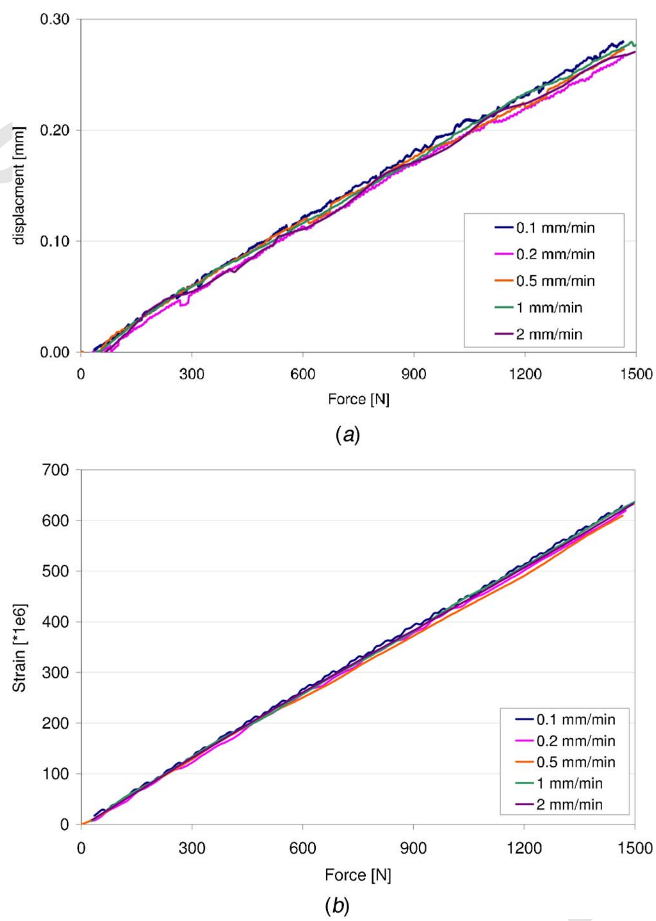


**Fig. 11 Fresh-frozen femur shows insensitive behavior to different strain rates (at 7 deg inclination): head's displacement vis. load (*a*) and neck superior strain vis. load (*b*)**



PROOF COPY [BIO-06-1060] 001703JBY

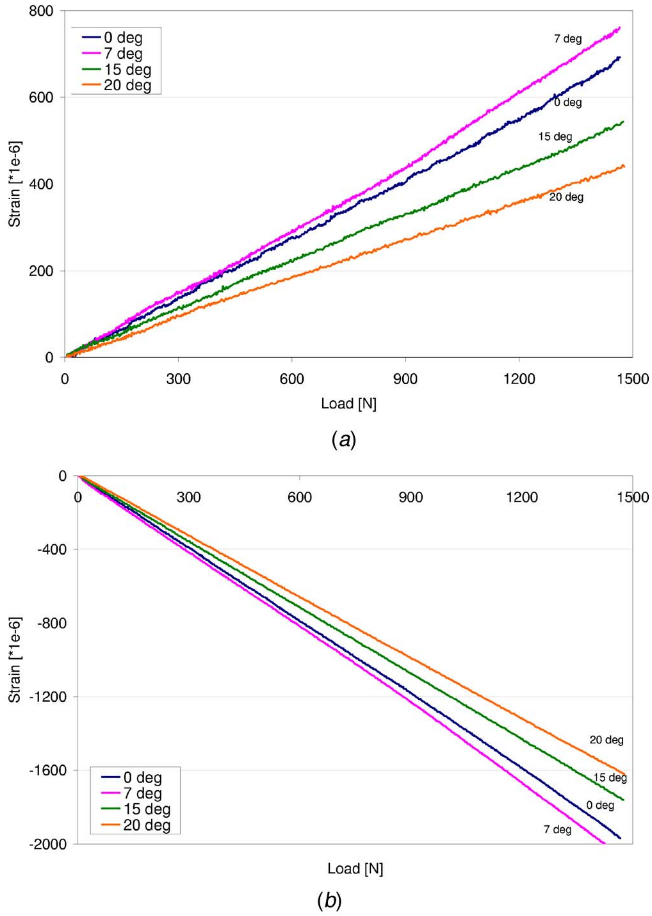


**Fig. 12 Inclination angle influence on strains at neck superior (*a*) and inferior (*b*)**

vertical posture was observed (Fig. 12). This was most likely caused by measurement error. This behavior was also seen in displacements measured by the LVDT.

*3.1.5 Displacements and Strains*. Linear displacement/load ($\Delta z/\Delta F$) and strain/load ($\Delta\varepsilon/\Delta F$) ratios were computed for the experiment values and used for comparison purposes with FE linear analysis results. The ratios are computed using linear regression based on the linear response range only (between 200 N to maximum load).

In Table 2 we summarize the displacement at the load location in the $z$ direction divided by the applied load ($\Delta z/\Delta F$) (mean values) as measured by the LVDT. In this table $n$ is the number of valid experimental data considered. Note that the repeatability of the displacements/force measurements is within ±17% of the mean, except for the experiment at 7 deg inclination. The experiment at 7 deg inclination has a bad repeatability, thus will be included only for completeness of presentation but ignored from our analysis and discussion.

Table 2 summarizes the mean values of strain/force response at the different locations. At the neck superior, neck inferior, and shaft medial locations, the measured uniaxial strain is reported. At the shaft lateral location the principle strains computed from the rosette measurements are reported.

*3.1.6 Summary of the Experimental Results*. The fresh-frozen femur response showed good linearity and repeatability. The visco-elastic behavior does not seem to have significant influence on the monotonic loading beyond the force of 200 N. Most of the collected data present an expected characteristic behavior. This indicates that the results may be used for comparison with the FEA.

An unclear response at 7 deg inclination relative to 0 deg inclination, and an uncertainty in the displacement measurements suggests that the test results for 7 deg is unreliable.

### 3.2 Fresh-Frozen Proximal Femur FE Model

*3.2.1 FE Model Verification*. The discretization error inherent in the FE model was investigated by increasing the polynomial degree of the shape functions from 1 to 5 over three different meshes with $\approx 4200 - \approx 6000$ elements. The resultant force showed a small difference of 3.2% between the finest and coarsest meshes at $p=5$ (Fig. 13(*a*)).

To the best of our knowledge, the determination of the Young's modulus as a spatial field based on averaged data using moving average methods has not been investigated in the past. Therefore, it was important to investigate the results sensitivity to the volume of the box used for the averaging process. This investigation was performed separately for the trabecular and cortical regions. Three sets of spatial fields were determined according to three different volume sizes for moving average calculations on trabecular bone. The different volumes were $(3\times3\times3)$, $(5\times5\times5)$ and $(7\times7\times7)$ voxels boxes. This corresponds to box specimen with edge sizes of about 2.3–5.5 mm. The smaller size is similar to typical elements size used in $h$-FE models [1,2], while the bigger size is similar to reported test specimens (small) size. Material assignment used the (t.4) and (c.2) relationships in Table 1, based on the different approximated spatial fields (one for each moving average box size). This comparison was on the basis of bone's model at 0 deg inclination, using the 5100 element mesh with $p=5$. Surprisingly, averaging trabecular bone data according to different moving average box sizes did not show any significant effect on the analysis results (Fig. 13(*b*)). The resultant forces were almost the same for all three box sizes, with less than 1% difference (6662 N for $7\times7\times7$ voxels box versus 6713 N for $3\times3\times3$ voxels box ). Displacements and strains at several points agreed with less than 5% difference between models with different moving average box size. The sensitivity of the different relations $E(\rho_{app})$ in Subsection 2.2 as Wirtz et al., etc., was investigated on the FE model at 0 deg inclination (the density's spatial field and all other model definitions remain unchanged). Different $E(\rho_{app})$ relationships yielded significant differences in the FE results (Fig. 14). The resultant force using Wirtz's relations was almost twice that compared to Keller's relation (6662 N vis. 3381 N, respectively). As shall be discussed in the following section, the relations which best predicted the experimental displacement under a given load and at the same time distinguished between cortical and trabecular bone was (t.8) and (c.4) denoted as Cody et al. [27].

To check the sensitivity of the Poisson's ratio we examined values of 0.3, 0.35, and 0.4. We observed negligible influence when displacements or maximal principle strains were of interest. Only the transverse principle strains were slightly influenced.

We found that the height of the trimmed planar face on which the load is applied (see Figs. 1 and 5) had a significant influence on the final result. This height may be estimated to an accuracy of ±1 mm, with a CAD software or from pictures taken during the experiment, due to the difficulty of exactly determining where the conic jig contacted the bone. To determine the sensitivity of the analysis to this height, we ran the analysis under a homogeneous material assumption ($E=1000$ MPa, $\nu=0.4$). Three different models with planar trimmed face at 3 mm intervals were considered. The computed resultant force showed large sensitivity to the trimmed surface height with ≈30% difference between lowest and highest surface heights (the higher the planar trimmed face, the lower is the resultant force). The reason is that the higher the trimmed surface is, the resultant force approaches the shaft so a smaller moment is applied. The trimmed face height sensitivity increased by 33% (to 46%) after heterogeneous material proper-



PROOF COPY [BIO-06-1060] 001703JBY

**Table 2 Head's displacement/force ($\mu$m/N) response according to LVDT and strain/force ($\mu$ strain/N) at four locations for different bone inclination angles**

| Angle (deg) | Head's displacement/force ($\mu$m/N) | | | | | Neck superior: strain/force ($\mu$ strain/N) | | | | |
|---|---|---|---|---|---|---|---|---|---|---|
| | $n$ | Mean | Min | Max | $\Delta$ (%) | $n$ | Mean | Min | Max | $\Delta$ (%)[a] |
| 0 | 5 | 30.1 | 25.3 | 35.4 | 16.8 | 6 | 44.1 | 41.9 | 46.5 | 5.2 |
| 7 | 9 | 12.3 | 7.9 | 20.4 | 50.1 | 13 | 48.5 | 44.9 | 52.1 | 7.5 |
| 15 | 9 | 17.5 | 15.5 | 20.9 | 15.4 | 10 | 36.6 | 35.5 | 38.0 | 3.4 |
| 20 | 9 | 16.7 | 14.3 | 20.1 | 17.4 | 10 | 30.2 | 29.0 | 32.8 | 6.3 |

| Angle (deg) | Neck inferior: strain/force ($\mu$ strain/N) | | | | | Shaft medial: strain/force ($\mu$ strain/N) | | | | |
|---|---|---|---|---|---|---|---|---|---|---|
| | $n$ | Mean | Min | Max | $\Delta$ (%) | $n$ | Mean | Min | Max | $\Delta$ (%)[a] |
| 0 | 6 | −127 | −134 | −113 | 8.3 | 6 | −130 | −137 | −124 | 5.0 |
| 7 | 13 | −134 | −140 | −113 | 10.1 | 13 | −126 | −137 | −114 | 9.1 |
| 15 | 10 | −120 | −123 | −113 | 4.2 | 10 | −74.2 | −78.5 | −72.4 | 4.1 |
| 20 | 10 | −111 | −113 | −110 | 1.3 | 10 | −45.3 | −49 | −43.2 | 6.4 |

| Angle (deg) | Shaft lateral $\varepsilon_1$: strain/force ($\mu$ strain/N) | | | | | Shaft lateral $\varepsilon_3$: strain/force ($\mu$ strain/N) | | | | |
|---|---|---|---|---|---|---|---|---|---|---|
| | $n$ | Mean | Min | Max | $\Delta$ (%) | $n$ | Mean | Min | Max | $\Delta$ (%)[a] |
| 0 | 6 | 44.0 | 40.7 | 47.3 | 7.5 | 6 | −14.6 | −15.3 | −13.8 | 5.1 |
| 7 | 13 | 40.9 | 38.8 | 44.2 | 6.6 | 13 | −14.4 | −15.2 | 0.5 | 54.5 |
| 15 | 10 | 25.3 | 24.2 | 27.1 | 5.7 | 10 | −9.2 | −9.8 | −8.7 | 6.0 |
| 20 | 10 | 16.8 | 15.9 | 17.9 | 5.9 | 10 | −6.3 | −6.7 | −5.8 | 8.7 |

[a] $\Delta(\%)=100^{*}(\max-\min)/(2\times \text{mean})$.

ties were assigned. Examining a more complicated, yet more realistic cone shaped face for the contact surface showed only a small difference from the trimmed planar surface and therefore discarded. A representative stress field within the bone is provided in Fig. 15 in which we show the von Mises stress in MPa for the 0 deg inclination bone at 1500 N load. The bone is sliced at the end of the cortical zone region in the right half of the figure. There is an expected jump in stresses over the interface of the trabecular/cortical interface in the bone under the cut section, whereas in the upper part the stress field is smooth because no cortical region is represented in the bone's head. The location of largest stress is in an expected location at the bottom of the bone's neck.

*Model Validation by Experimental Observations*. To mimic the boundary conditions on femur's head in the experiment we applied a uniform pressure over the entire trimmed planar surface in the axial direction while constraining the displacements perpendicular to the load direction. The resultant force of the pressure (in $z$ direction) equals 1500 N as in the experiment. The constrains on the displacements in $x$ and $y$ directions on the surface on which load is applied results, for example in the bone at 0 deg inclination, in a reaction of 551 N and 41 N in $x$ and $y$ directions and a moment of $(M_x, M_y, M_z)=(23,27,-28)$ N mm around the midpoint of the surface. Because the pressure results in a nonuniform displacement field on that plane, we averaged the displacement field extracted from the FE analysis (to be compared with the experimental measurements) over two lines passing through the center of area. From the different relationships $E(\rho_{\text{app}})$ considered in Subsection 3.2, the one defined by Cody et al. provided the closest results compared to the experimental observations, and results reported in the following were obtained by using Cody et al. relationship.

A good prediction was achieved for two out of the four inclination angles, (Table 3 and Fig. 16). An almost accurate prediction

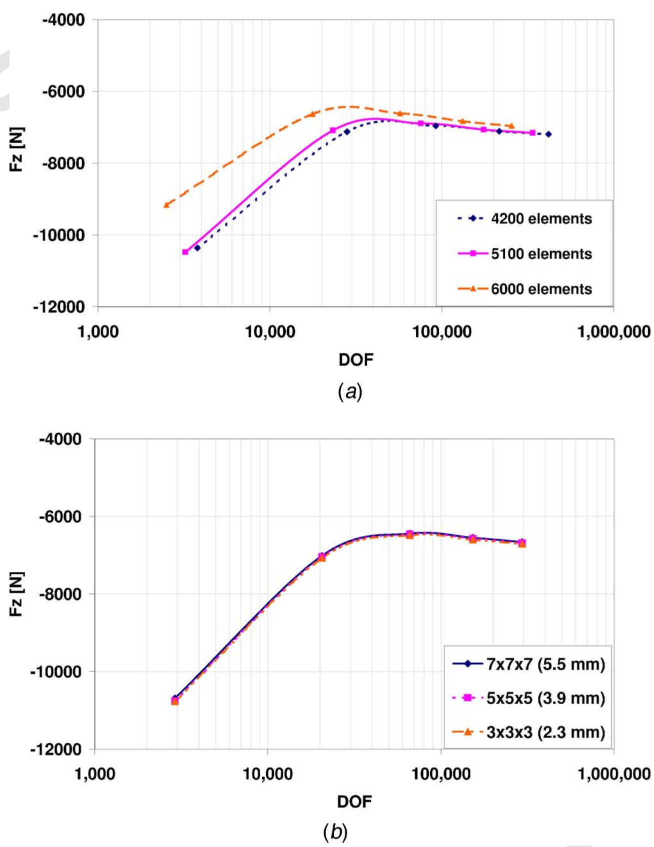


**Fig. 13 Resultant force ($Fz$) versus degree of freedom (DOF) under head displacement of 1 mm (0 deg tilt): ($a$) influence of different FE meshes and ($b$) moving average box sizes**

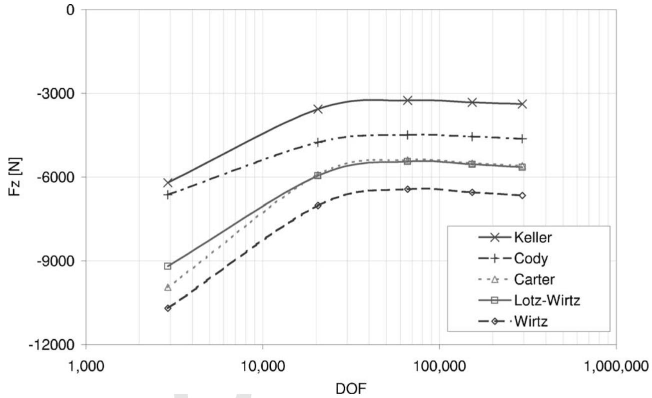


**Fig. 14 Resultant force [$N$] due to head displacement of 1 mm for 0 deg inclination angle: convergence of FEA resultant force according to several $E(\rho_{app})$ relations**

was obtained for load configuration of 15 deg and 20 deg, whereas for 0 deg a discrepancy exists. The experimental results for an inclination 7 deg are known to be questionable.

We concluded that the predicted FE displacements were in very good agreement with the experimental observations, because the experimental error in the displacement was about 15% and for 7 deg was about 50%.

In addition, we compared the FE strains and those measured in the experiment at the four different locations (Table 3). A closer correlation of the results was observed in the neck area than along the shaft. Even the relatively high difference of up to 66% at the neck superior location was considered to be in reasonable agreement compared to reported results by others [15,30]. However, the FE strains along the shaft were not in good agreement with these measured in experiments.

## 4 Discussion

FE simulations include *idealization errors* introduced by assumptions made to describe a physical system by mathematical models and *discretization errors* introduced by solving the mathematical equations by numerical methods. $p$-FEA of the femur allowed us to keep the discretization errors under control and enabled us to focus on the physical phenomena, trying to validate the FE results by comparing displacements and strains to in-vitro experimental observations. Idealization errors associated with realistic representation of the geometry, boundary conditions and material properties determination and assignment were among the most important errors investigated. To this end, the presented $p$-FE model had several characteristics: (a) outer boundary of the bone was represented by smooth surfaces; (b) cortical and trabecular regions were separated by a surface; and (c) inhomogeneous Young's modulus was represented by continuous piecewise polynomial functions. These are believed to reduce the idealization errors and at the same time these definitely reduced numerical errors.

The geometric FE representation depends on the CT resolution, the smooth surface approximation, and the FE mapping. The first two have together an effect of less than 1 mm, taking into account a half pixel size plus the reported surface mean approximation error. This should not have a major effect on the model geometry

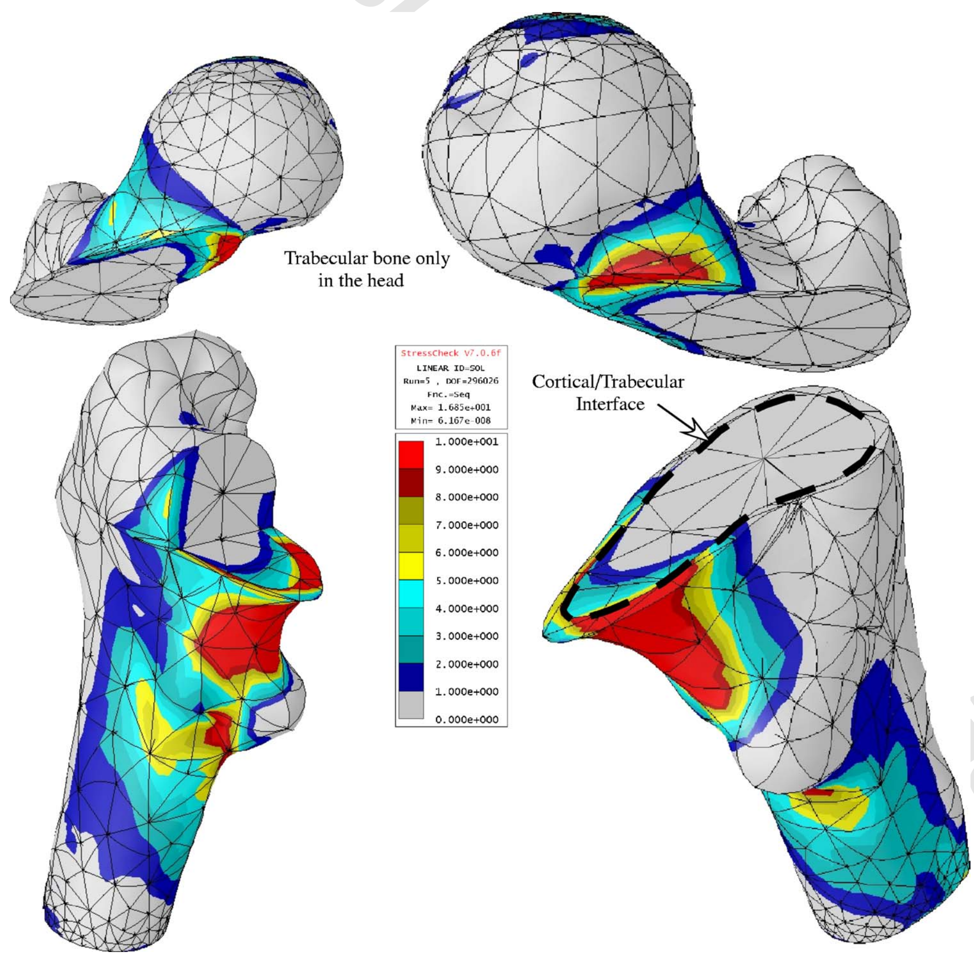


**Fig. 15 von Mises stress (MPa) for a 1500 N load in the bone at 0 deg inclination angle**



PROOF COPY [BIO-06-1060] 001703JBY

**Table 3 Displacements (mm) and strains ($\mu$ strain) at 1500 N load: FEA results using Cody et al. relations and experimental measurements (%Δ refers to experimental measurement)**

| Angle (deg) | Head displacement (mm) FEA | Head displacement (mm) Exp. | Head displacement Δ (%) | Strain at neck superior FEA | Strain at neck superior Exp. | Strain at neck superior Δ (%) | Strain at neck inferior FEA | Strain at neck inferior Exp. | Strain at neck inferior Δ (%) |
|---|---|---|---|---|---|---|---|---|---|
| 0 | 0.35 | 0.45 | −22 | 1058 | 662 | 60 | −1874 | −1954 | −4 |
| 7 | 0.30 | 0.19 | 58 | 916 | 743 | 23 | −1813 | −2029 | −11 |
| 15 | 0.28 | 0.26 | 8 | 807 | 549 | 47 | −1766 | −1806 | −2 |
| 20 | 0.26 | 0.25 | 4 | 750 | 453 | 66 | −1744 | −1662 | 5 |

| Angle (deg) | Strain at shaft medial FEA | Strain at shaft medial Exp. | Strain at shaft medial Δ (%) | Strain at shaft lateral ($\epsilon_1$) FEA | Strain at shaft lateral ($\epsilon_1$) Exp. | Strain at shaft lateral ($\epsilon_1$) Δ (%) |
|---|---|---|---|---|---|---|
| 0 | −359 | −1955 | −82 | 168 | 660 | −75 |
| 7 | −151 | −1944 | −92 | 91 | 617 | −85 |
| 15 | 68 | −1112 | −106 | 57 | 380 | −85 |
| 20 | 182 | −679 | −127 | 55 | 252 | −78 |

$\Delta\% = 100^{*}(\text{FEA} - \text{Exp})/\text{Exp}$.

and therefore on the displacement results. The FE mapping was investigated (a finer mesh size and different mapping functions) and found to have negligible influence on the displacement results and strains.

Determination of bone density from CT scans, the density averaging algorithm, and follow on approximation by LMS polynomials are sources of idealization errors that deserve to be discussed. The quality of the CT scan data introduces inaccuracies in the density. Different brands of scanners use different reconstruction algorithms, so each provides different degrees of accuracy with respect to measuring bone density. This is a topic which was not addressed in our study, but is believed to have second-order effects on the results. Averaging the density for computational purposes was an accepted practice in many bone FE applications, however, applying a moving average technique was not widely accepted in other studies. In our approach density at each point was mesh independent determined by its close surrounding, rather than by voxels that were enclosed in the same element, and the averaging box size was determined to have the same volume as specimens used for the $E(\rho_{\text{app}})$ relationship.

The prediction of the mechanical response of the femur depends on the ability to approximate the density by continuous functions. Large variations of density along the entire trabecular bone necessitated the use of several different functions to approximate it (three different functions in distinct regions). The discontinuity of functions along the regions borders introduced discontinuity in strain field computed by FEs at some locations along the borders. Nevertheless, the strain-gauge location in the test were at least two elements away from these borders and therefore this problem should not cause the large discrepancies in the strains. This issue will be addressed in a future work. The evaluated density functions showed good approximation to the raw CT based values with $R^2 > 0.97$. Nevertheless, further investigation will be undertaken to examine if bases other than polynomials and trigonometric functions may provide a better approximation. In this research, higher polynomial degrees of the LMS approximation lead to ill-conditioned matrices. Therefore, the separation between cortical and trabecular regions is deemed to be essential due to different functional representation and to obtaining well-conditioned matrices, necessary to reliably evaluate the unknown coefficients representing the function. We conclude that the spatial field representation cannot be straightforwardly implemented in other structure based meshing methods such as Refs. [18,23]. Other complications could rise due to high density gradients in the osteoporotic region, but in this case several fields can be used, e.g., one for the healthy trabecular region and another for the osteoporotic one. The LMS approximation of the density is a significant unknown. At first, it did not seem to have a big influence on the FE results—changing the box size used for averaging did not result in large changes in the FE solution. However, additional numerical experiments are necessary to establish how averaging affects the results.

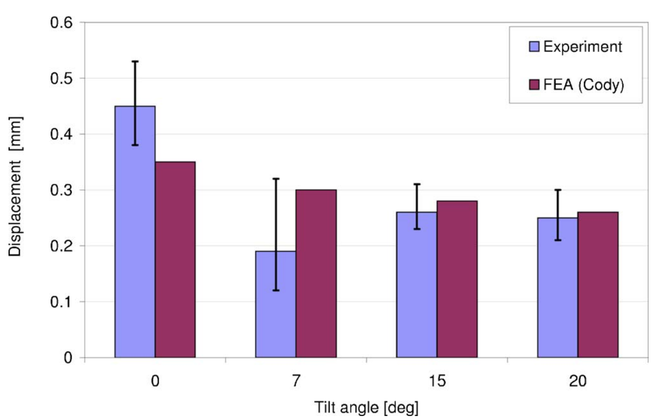


**Fig. 16 FEA results using Cody et al. relations compared to experimental observations: Femur head displacement at 1500 N compression at several inclination angles (error bars indicate min. and max. measured values)**

In this respect, it is worthwhile to mention a recent numerical study [41] in which FE results obtained by voxel-based methods were compared with the method presented herein. Several domains with increased complexity were considered to evaluate the influence of: (a) accurate surface representation; (b) continuous material representation; and (c) element size. The results showed that both methods were in qualitative agreement. Nevertheless, our method showed a more realistic strain field and almost constantly lower displacements and strains compared to the voxel-based models. Also, the separation between the cortical and trabecular regions introduced a stiffer behavior of the $p$-FEM model because of reducing the underestimated cortical shell stiffness due to the average with trabecular density or air (near surface). These results were consistent with Ref. [1], in which all structure-based models investigated show 15% stiffer response compared to the voxel-based model. Underestimation of bone Young's modulus in voxel based methods was also described by Ref. [25] and considered to be important.

The separation of the bone into cortical and trabecular regions introduced three sources of inaccuracies: (a) neglecting the cortical shell above lesser trochanter; (b) position of separating border; and (c) thickening of the cortical shell near the lesser trochanter. The influence of the three is difficult to assess. In our opinion, neglecting the thin cortical shell (0.1–0.4 mm) may affect the local strains, but not the global displacement. The inaccurate separation of the surface and cortical shell thickening may introduce errors. However, the use of the cortical relation (c.4) instead of the trabecular one (t.8) on a low density region having $\rho_{app} < 1.2\ g/cm^3$, leads to lower Young's modulus evaluation and therefore could not introduce the stiffer response shown by the model.

The determination of the elastic parameters is of major importance in assessing idealization errors. This was numerically investigated with various $E(\rho_{app})$ relations and a number of $\nu$ values. Young's modulus determination based on the CT data includes two types of errors: one results from the computation of $\rho_{app}(HU)$ and the other from the relation $E(\rho_{app})$. Even if one considers the relation $\rho_{app}(HU)$ to be estimated with $R^2 \geq 0.8$, and $E(\rho_{app})$ to be estimated with $R^2 \geq 0.8$, then $E(HU)$ obtained by using the two relations applied consequently may have a quite low correlation quality (yet both Refs. [39,5] report on good correlation of $E(HU)$). We found that using a specific relation for $E(\rho_{app})$ can cause a 100% error in the displacement/force results alone.

The excellent linear response observed in the experiment complies with the linear elastic assumption, and the visco-elastic response as measured during monotonic loading was negligible. The bone response was insensitive to changes in strain rates in the range 0.1–2 mm/min. However, we found that the isotropic assumption can indeed overestimate bone stiffness. The bone stiffness in the principal strain was reported to be 1.7–2.5 times stiffer than in the transverse direction [5,7,39]. Although one may want to correlate the FE errors to that assumption alone, one must not forget that the bone is assumed to be remodeled such that for the experiment configuration (similar to stance posture) the material principal directions are oriented according to principal stresses, thus uniaxial properties may be satisfactory [42]. Nevertheless, the influence of transversely isotropic material properties on the results will be investigated in a future study.

We thus conclude that a large experimental database of FEA studies is necessary to identify the best $E(\rho_{app})$ relationship. The relationship used by Ref. [27] was found to provide close results as measured in the experiment. Poisson's ratio, on the other hand, had almost no effect on the results. The strain measurements (a property found to be affected) were taken from nearly the principal direction and therefore should not be largely influenced by the arbitrary Poisson's ratio used.

Finally, to evaluate experimental errors, it was important to consider the experimental data as a reference. The load and strains measurement errors were by far less significant than all other errors considered. However, the errors in the position and orientation of the strain gauges were about ±0.8 mm and about 16 deg. Such errors may affect the result comparison. It was impossible to know which one is more reliable, so a definite model assessment cannot be done. An error in bone inclination angle measurement was addressed (although not described here) resulting in less than 2% difference in displacement due to a 1 deg inclination error.

An important observation in the FE model was the large strain gradients in the areas of interest. These large gradients in strain may be attributed to one of the following: (1) the geometrical irregularity of the surface; and (2) the spatial field functional representation and several very distorted elements. For example, the FE principal strains at the location of the rosette show a difference of 78% between the upper and lower ends of the rosette. Such differences make it difficult to correlate predicted to measured strains.

The low FE strains in the shaft (compared to the experimental observations) may be a result of overestimation of the Young's modulus in the cortical regions, either due to the $E(\rho_{app})$ relation or to overestimation of $\rho_{app}$ from CT scans. These discrepancies have to be further investigated by a larger experimental database.

To conclude, the model presented in this paper has been numerically verified and found to have good displacement prediction. Although it cannot yet be fully validated because of the strains prediction, the errors reported in this study are quite reasonable in view of past experiments of the proximal femur. We found that the two main factors that mostly influence the FEA reliability are the material properties assignment (both Young's modulus evaluation and isotropic assumption) and the determination of the exact area subject to load. Both will be further investigated in the future to improve the analysis reliability. Also, one has to keep in mind that the comparison herein is based on a single tested bone. Other specimens may produce different results and therefore a larger experimental database has to be generated (consisting of several bones) and further FE analyses incorporating transversely isotropic material properties are required which may have a prominent influence on the results.

## 5 Summary

A new method was described for a more reliable simulation of the mechanical response of bones based on the smooth representation of bone's geometry, separating the trabecular and cortical region, considering a spatial description of the inhomogeneous Young's modulus, and a high order FE analysis. The thrust behind the new method stems from the desire to represent the bone geometry more accurately and from the desire to improve the evaluation of mechanical properties with experimental methods that were used to generate the correlations between QCT and mechanical properties. The resulting structured-based method showed superior performance compared to the common voxel-based method.

Model verification and validation against experimental results show good prediction for the displacements due to load at three out of four inclination angles, and strains at two locations. Strain's FE prediction at the other two locations were not in good correlation with the experimental observations. This model prediction will probably improve with the use of transversely isotropic material properties for the cortical bone, to enable a more realistic simulation of the mechanical response of the femur.

Finally, as a service to the research community, we have made publicly available CT scans and FE mesh of the fresh-frozen bone as a download at the URL address: www.bgu.ac.il/~zohary/CT_FF.html AQ: #2

## Acknowledgment

The authors thank Dr. Ariel Simkin and Mr. Ilan Gilad for their assistance with the in-vitro experiments and Mr. Nir Trabelsi for his help with data processing.

## Nomenclature

| | | |
|---|---|---|
| FE | = | finite elements |
| FEA | = | finite element analysis |
| FEM | = | finite element method |
| $h$-FEM | = | conventional FEM: convergence achieved by reducing element size keeping low polynomial order over elements |
| HU | = | Hounsfield units in CT scans associated with density |
| LMS | = | least mean squares |
| $p=1$ | = | polynomial order over a finite element is 1 |
| $p$-FEM | = | high-order FEM: convergence achieved by increasing polynomial order over elements |
| QCT | = | quantitative computerized tomography |

## References


[1] Viceconti, M., Bellingeri, L., Cristofolini, L., and Toni, A., 1998, "A Comparative Study on Different Methods of Automatic Mesh Generation of Human Femurs," Med. Eng. Phys., **20**, pp. 1–10.

AQ: #3 [2] Taddei, F., Cristofolini, L., Martelli, S., Gill, H. S., and Viceconti, M., 2006, "Subject-Specific Finite Element Models of Long Bones: An In vitro Evolution of the Overall Accuracy," J. Biomech., in press.

[3] Keaveny, T. M., Guo, E., Wachtel, E. F., McMahon, T. A., and Hayes, W. C., 1994, "Trabecular Bone Exhibits Fully Linear Elastic Behavior and Yields at Low Strains," J. Biomech., **27**, pp. 1127–1136.

[4] Cowin, S. C., and Ashby, M. F., 2001, *Bone Mechanics Handbook*, CRC Press, Boca Raton, FL.

[5] Lotz, J. C., Gerhart, T. N., and Hayes, W. C., 1991, "Mechanical Properties of Metaphyseal Bone in the Proximal Femur," J. Biomech., **24**, pp. 317–329.

[6] Lotz, J. C., Gerhart, T. N., and Hayes, W. C., 1990, "Mechanical Properties of Trabecular Bone from the Proximal Femur: A Quantitative CT Study," J. Comput. Assist. Tomogr., **14**(1), pp. 107–114.

[7] Wirtz, D. C., Schiffers, N., Pandorf, T., Radermacher, K., Weichert, D., and Forst, R., 2000, "Critical Evaluation of Known Bone Material Properties to Realize Anisotropic FE-Simulation of the Proximal Femur," J. Biomech., **33**, pp. 1325–1330.

[8] Morgan, E. F., Bayraktar, H. H., and Keaveny, T. M., 2003, "Trabecular Bone Modulus-Density Relationships Depend on Anatomic Site," J. Biomech., **36**, pp. 897–904.

[9] Keller, T. S., 1994, "Predicting the Compressive Mechanical Behavior of Bone," J. Biomech., **27**, pp. 1159–1168.

[10] Rho, J. Y., Hobatho, M. C., and Ashman, R. B., 1995, "Relations of Mechanical Properties to Density and CT Numbers in Human Bone," Med. Eng. Phys., **17**, pp. 347–355.

[11] Szabó, B. A., and Babuška, I., 1991, *Finite Element Analysis*, Wiley, New York.

[12] Mueller-Karger, C. M., Rank, E., and Cerrolaza, M., 2004, "p-Version of the Finite Element Method for Highly Heterogeneous Simulation of Human Bone," Finite Elem. Anal. Design, **40**, pp. 757–770.

[13] Keyak, J. H., Rossi, S. A., Jones, K. A., and Skinner, H. B., 1998, "Prediction of Femoral Fracture Load Using Automated Finite Element Modeling," J. Biomech., **31**, pp. 125–133.

[14] Cody, D. D., Gross, G. J., Hou, F. J., Spencer, H. J., Goldstein, S. A., and Fyhrie, D. P., 1999, "Femoral Strength is Better Predicted by Finite Element Models than QCT and DXA," J. Biomech., **32**, pp. 1013–1020.

[15] Lotz, J. C., Cheal, E. J., and Hayes, W. C., 1991, "Fracture Prediction for the Proximal Femur Using Finite Element Models: Part 1—Linear Analysis," J. Biomech. Eng., **113**, pp. 353–360.

[16] Mertz, B., Niederer, P., Muller, R., and Ruegsegger, P., 1996, "Automated Finite Element Analysis of Excised Human Femura Based on Precision-QCT," J. Biomech. Eng., **118**, pp. 387–390.

[17] Wirtz, D. C., Pandorf, T., Portheine, F., Radermacher, K., Schiffers, N., Prescher, A., Weichert, D., and Firtz, U. N., 2003, "Concept and Development of an Orthotropic FE Model of the Proximal Femur, J. Biomech., **36**, pp. 289–293.

[18] Couteau, B., Payan, Y., and Lavallee, S., 2000, "The Mesh-Matching Algorithm: An Automatic 3d Mesh Generator for Finite Element Structures," J. Biomech., **33**, pp. 1005–1009.

[19] Keyak, J. H., Meagher, J. M., Skinner, H. B., and Mote, C. D. Jr., 1990, "Automated Three-Dimensional Finite Element Modelling of Bone: A New Method," J. Biomed. Eng., **12**, pp. 389–397.

[20] Cody, D. D., McCubbrey, D. A., Divine, G. W., Gross, G. J., and Goldstein, S. A., 1996, "Predictive Value of Proximal Femural Bone Densiometry in Determining Local Orthogonal Material Properties," J. Biomech., **29**, pp. 753–761.

AQ: #4 [21] Fox, J. C., Gupta, A., Blumenkrantz, G., Bayraktar, H. H., and Keaveny, T. M., 2004, "Role of Elastic Anisotropy and Failure Criterion in Femoral Fracture Strength Predictions," Trans. Orthopaedic Res. Soc., ■■, pp. 520–■.

[22] Marom, A. S., and Linden, M. J., 1990, "Computer Aided Stress Analysis of Long Bones Utilizing Computed Tomography," J. Biomech., **23**, pp. 399–404.

[23] Viceconti, M., Davinelli, M., Taddei, F., and Cappello, A., 2004, "Automatic Generation of Accurate Subject-Specific Bone Finite Element Models to be Used in Clinical Studies," J. Biomech., **37**, pp. 1597–1605.

[24] Taddei, F., Pancanti, A., and Viceconti, M., 2004, "An Improved Method for the Automatic Mapping of Computed Tomography Numbers Onto Finite Element Models," Med. Eng. Phys., **26**, pp. 61–69.

[25] Zannoni, C., Mantovani, R., and Viceconti, M., 1998, "Material Properties Assignment to Finite Element Models of Bone Structure: A New Method," Med. Eng. Phys., **20**, pp. 735–740.

[26] Esses, S. I., Lotz, J. C., and Hayes, W. C., 1989, "Biomechanical Properties of the Proximal Femur Determined In Vitro by Single-Energy Quantitative Computed Tomography," J. Bone Miner. Res., **4**, pp. 715–722.

[27] Cody, D. D., Hou, F. J., Divine, G. W., and Fyhrie, D. P., 2000, "Short Term In Vivo Study of Proximal Femoral Finite Element Modeling," Ann. Biomed. Eng., **28**, pp. 408–414.

[28] Yang, G., Kabel, J., VanRiertbergen, B., Odgaard, A., Huiskes, R., and Cowin, S. C., 1999, "The Anisotropic Hooke's Law for Cancellous Bone and Wood," J. Elast., **53**, pp. 125–146.

[29] Keyak, J. H., and Skinner, H. B., 1992, "Three-Dimensional Finite Element Modelling of Bone: Effect of Element Size," J. Biomed. Eng., **14**, pp. 483–489.

[30] Keyak, J. H., Fourkas, M. G., Meagher, J. M., and Skinner, H. B., 1993, "Validation of Automated Method of Three-Dimensional Finite Element Modelling of Bone," J. Biomed. Eng., **15**, pp. 505–509.

[31] Yeni, Y. N., and Fyhire, D. P., 2001, "Finite Element Calculated Uniaxial Apparent Stiffness is a Consistent Predictor of Uniaxial Apparent Strength in Human Vertebral Cancellous Bone Tested with Different Boundary Conditions," J. Biomech., **34**(12), pp. 1649–1654.

[32] Templeton, A., and Liebschner, M., 2004, "A Hierarchical Approach to Finite Element Modeling of the Human Spine," Crit. Rev. Eukaryot Gene Expr, **14**(4), pp. 317–328.

[33] Hernandez, C. J., Gupta, A., and Keaveny, T. M., 2006, "A Biomechanical Analysis of the Effects of Resorption Cavities on Cancellous Bone Strength," J. Bone Miner. Res., **21**(8), pp. 1248–1255.

[34] Kenney, J. F., and Keeping, E. S., 1962, *Mathematics of Statistics*, Van Nostrand, New York.

[35] Ayyub, B. M., and McCuen, R. H., 1996, *Numerical Methods for Engineers*, Prentice Hall, Englewood Cliffs, NJ.

[36] Padan, R., 2006, "Towards a Reliable Mechanical Simulation of the Proximal Femur," M.Sc. thesis, Ben-Gurion University of the Negev, Beer-Sheva, Israel.

[37] Rice, J. C., Cowin, S. C., and Bowman, J. A., 1988, "On the Dependence of the Elasticity and Strength of Cancellous Bone on Apparent Density," J. Biomech., **21**, pp. 155–168.

[38] Carter, D. R., and Hayes, W. C., 1977, "The Compressive Behavior of Bone as a Two-Phase Porous Structure," J. Bone Jt. Surg., Am. Vol., **59**, pp. 954–962.

[39] Ciarelli, M. J., Goldstein, S. A., Kuhn, J. L., Cody, D. D., and Brown, M. B., 1991, "Evaluation of Orthogonal Mechanical Properties and Density of Human Trabecular Bone From the Major Metaphyseal Regions With Materials Testing and Computed Tomography," J. Orthop. Res., **9**, pp. 674–682.

[40] Jensen, J. S., 1978, "A Photoelastic Study of a Model of the Proximal Femur. A Biomechanical Study of Unstable Trochanteric Fractures I," Acta Orthop. Scand., **49**(1), pp. 54–59.

[41] Fedida, R., Yosibash, Z., Milgrom, C., and Joscowicz, L., 2005, "Femur Mechanical Simulation Using High-Order FE Analysis With Continuous Mechanical Properties," *Proceedings of ICCB05 - II International conference on computational bioengineering*, Lisbon, Portugal, Vol. 1, H. Rodrigues et al., eds., IST Press, pp. 85–96.

[42] Keyak, J. H., and Rossi, S. A., 2000, "Prediction of Femoral Fracture Load Using Finite Element Models: An Examination of Stress- and Strain-Based Failure Theories," J. Biomech., **33**, pp. 209–214.

**AUTHOR QUERIES — 001703JBY**

#1 AQ: zip?

#2 AQ: Convert this to a Ref. Give author(s), year, title of page.

#3 AQ: update Ref. 2.

#4 AQ: Provide volume number and page range for Ref. 21.